Article

Ferroelectric incommensurate spin crystals

https://doi.org/10.1038/s41586-021-04260-1

Received: 8 March 2021

Accepted: 17 November 2021

Published online: 9 February 2022

Check for updates

Dorin Rusu[1], Jonathan J. P. Peters[1,2], Thomas P. A. Hase[1], James A. Gott[1], Gareth A. A. Nisbet[3], Jörg Strempfer[4], Daniel Haskel[4], Samuel D. Seddon[1], Richard Beanland[1], Ana M. Sanchez[1] & Marin Alexe[1]✉

Ferroics, especially ferromagnets, can form complex topological spin structures such as vortices[1] and skyrmions[2,3] when subjected to particular electrical and mechanical boundary conditions. Simple vortex-like, electric-dipole-based topological structures have been observed in dedicated ferroelectric systems, especially ferroelectric–insulator superlattices such as $PbTiO_3/SrTiO_3$, which was later shown to be a model system owing to its high depolarizing field[4–8]. To date, the electric dipole equivalent of ordered magnetic spin lattices driven by the Dzyaloshinskii–Moriya interaction (DMi)[9,10] has not been experimentally observed. Here we examine a domain structure in a single $PbTiO_3$ epitaxial layer sandwiched between $SrRuO_3$ electrodes. We observe periodic clockwise and anticlockwise ferroelectric vortices that are modulated by a second ordering along their toroidal core. The resulting topology, supported by calculations, is a labyrinth-like pattern with two orthogonal periodic modulations that form an incommensurate polar crystal that provides a ferroelectric analogue to the recently discovered incommensurate spin crystals in ferromagnetic materials[11–13]. These findings further blur the border between emergent ferromagnetic and ferroelectric topologies, clearing the way for experimental realization of further electric counterparts of magnetic DMi-driven phases.

Despite the fundamental difference in the origin and strengths of internal magnetic and electric fields, similar dipolar topologies are apparent in both ferroelectrics and ferromagnets. The current understanding of what drives these topologies is based on the complex interplay between strain, electric and polarization gradient energies[14]. For example, polar vortices have been discovered in thin ferroelectric films and extensively studied in an environment that maximizes the depolarization field generated by the surface charges in ferroelectric–insulator superlattices[15–18]. The use of insulating layers, however, hinders the integration of such heterostructures into devices that could make use of the electronic characteristics of the complex topologies[19,20]. Ferroelectric heterostructures with metallic contacts, which are much easier to incorporate into devices, have—so far—been shown only to stabilize more common topologies, such as 180° domains with localized polar vortices at the domain walls[21] or flux-closure domains[22,23].

In magnetism, non-collinear spin interactions such as the Dzyaloshinskii–Moriya interaction (DMi) can trigger complex spin topologies that are incommensurate relative to the crystal structure of the host material. Such spin textures are described by several magnetic moment windings coexisting along several directions. Examples include chiral skyrmion lattices (double[11] or triple[24] **Q**) or the recently observed incommensurate spin crystal phases (isotropic/anisotropic double **Q**)[25]. Following the link between the topological dipole textures of ferroelectrics and ferromagnets, can this analogy be extended to multiple-**Q** incommensurate polarization textures? If it is possible, such a feat could hint towards the physical manifestation of an electric DMi, which has recently been shown to be allowed by symmetry[26]. In this work, we experimentally demonstrate ordered arrays of polar vortices in a single thin ferroelectric film with metallic boundary conditions. Unlike the vortex phases in $PbTiO_3$ (PTO)/$SrTiO_3$ (STO) superlattices, which show translational symmetry along the vortex core[4], we demonstrate a previously undescribed topology with an extra periodic perturbation along the vortex core that is an analogue of the double-**Q** magnetic spin crystal phase[25]. Motivated by the magnetic counterpart, we suggest either cycloidal or helical modulations as giving rise to this extra periodic perturbation. Our simulations and experimental data point towards a cycloidal winding.

Early theoretical results have shown that closure domains are very effective in minimizing depolarization fields in ultrathin films of $BaTiO_3$ (BTO) with $SrRuO_3$ (SRO) electrodes[27]. We have extended these studies within the density functional theory (DFT) framework and applied it to the similar PTO/SRO system, in which in-plane lattice strain is introduced through epitaxial matching to $DyScO_3$ (DSO). Bulk PTO has a much larger unit-cell dipole (~90 μC cm^{-2}) compared with BTO (~30 μC cm^{-2}), suggesting that a higher energy cost is associated with any dipole rotation. However, the polar map within the PTO layer, after relaxing the cation–oxygen octahedra, shows a continuous rotation of the local polarization that assembles into an ordered array of polar vortices, as seen in Fig. 1a. Thus, the large electrostatic energy is minimized by local rotations of surface dipoles, similar to ferromagnetic Kittel domains[27,28]. The DFT model suggests that this energy-minimization pathway is adopted even for metal-like boundary conditions such as those provided by SRO, which has a high charge density of around 2×10^{22} electrons cm^{-3} and a screening length of only around 1–2 Å (ref. [29]). Whilst, in principle, SRO should provide better screening than STO, our theoretical models show that it is still unable to screen the large

[1]Department of Physics, University of Warwick, Coventry, UK. [2]School of Physics, Trinity College Dublin, Dublin, Ireland. [3]Diamond Light Source, Didcot, UK. [4]Argonne National Laboratory, Lemont, IL, USA. ✉e-mail: M.Alexe@warwick.ac.uk

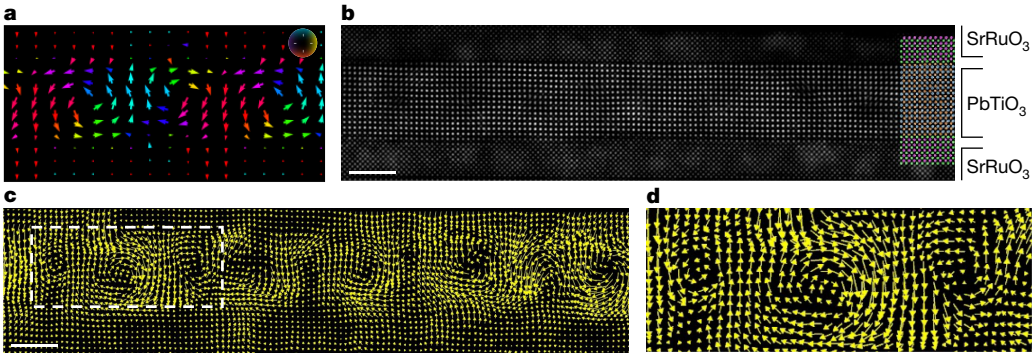

Fig. 1 | Unit-cell-scale electric dipole topologies. a, Relaxed cation–oxygen octahedra displacements map of the $(SrRuO_3)_{6.5}/(PbTiO_3)_{5.5}$ system from DFT, where 6.5 and 5.5 refer to the number of unit cells of the respective layer. **b**, ADF-STEM image showing the distortions within the $PbTiO_3$ layer. **c**, Unit-cell polarization map of the ADF-STEM image showing the local structure of the polarization pattern. **d**, Enlarged region marked by the dashed box in **c**, showing the vortices formed by the polar structure. The scale bars in **b** and **c** are 2.5 nm.

bound surface charges of the ferroelectric layer. Complex arrays of polarization vortices might therefore also be expected to develop in SRO/PTO/SRO structures.

Motivated by these promising DFT results, SRO/PTO/SRO trilayers were grown on STO-buffered DSO substrates. Atomic force microscopy (AFM) and transmission electron microscopy (TEM) studies confirm the structural quality of the sample (Extended Data Fig. 1). As PTO is a displacive ferroelectric, the polarization direction can be determined from the relative positions of the B-site cations and oxygen atoms[30]. Therefore the polarization can be mapped at a unit-cell level using aberration-corrected scanning transmission electron microscopy (STEM) (Fig. 1b). The experimentally determined polarization map shows an ordered array of polar vortices (Fig. 1c) within the ferroelectric layer. The main topological characteristics—that is, periodicity, off-centre core, clockwise/anticlockwise pairs etc.—are in good agreement with the DFT studies, despite the almost doubled thickness of the PTO layer in the experimental sample. The observed vortex pattern has a non-zero toroidal moment $\mathbf{G} = (2N)^{-1}\sum_i r_i \times P_i$, which is parallel to the vortex core. Here P_i is the local dipole moment located at r_i and N is the number of dipoles[31]. The formation of polar vortices, as highlighted in Fig. 1d, in which the local dipoles rotate in such a way to reduce both the depolarization and stray fields, avoids the suppression of the ferroelectricity in the thin films[32]. Furthermore, the STEM data show that the polarization topology is characterized by periodic pairs of clockwise–anticlockwise vortices, with a periodicity of about twice the thickness of the PTO film (~9–10 nm).

Any TEM analysis required to show domains on the nanometre level necessarily has a very limited field of view. To explore the macroscopic ordering of the polar domains more widely, we used X-ray diffraction (XRD). The periodic structural distortions caused by the polar domains will be apparent as satellite peaks in the vicinity of the layer Bragg peaks. Because these domains are within a thin PTO layer, any satellites will be extended in the reciprocal space direction normal to the substrate. A 3D reciprocal space map (RSM) was recorded in the vicinity of the $(002)_{pc}$ DSO reflections (Extended Data Fig. 2a), with Q_x, Q_y and Q_z coincident with the $[H00]_{pc}$, $[0K0]_{pc}$ and $[00L]_{pc}$ directions (where pc indicates pseudocubic indices). Satellites arising from periodic lattice distortions can be observed clearly in Fig. 2a–c. Streaks of satellite intensity, centred around $Q_z = 3.1$ Å^{-1} (layer Bragg peak) can be seen in the projections into the Q_z–Q_x and Q_z–Q_y planes (Fig. 2a, b), which become clearer when projected into the Q_x–Q_y plane (Fig. 2c). Surprisingly, instead of only one periodicity, we find a second periodicity coexisting within the PTO layer, perpendicular to the first. Along Q_x, the satellites are separated by $\Delta Q_x = 0.071(1)$ Å^{-1}, corresponding to an in-plane periodicity of 8.85(6) nm along the $[100]_{pc}$ direction. The periodicities in the $[010]_{pc}$ direction are less well defined, but have a separation of

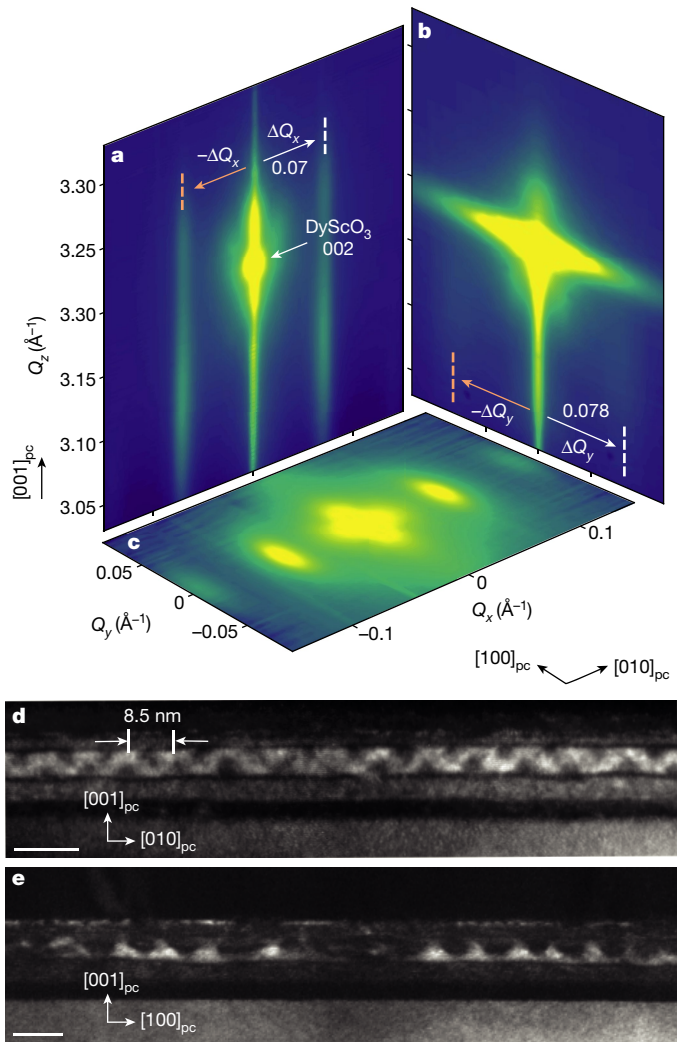

Fig. 2 | Macroscopic ordering. a, Q_z versus Q_x RSM. **b**, Q_z versus Q_y RSM along the perpendicular direction to that in **a**. **c**, Q_x versus Q_y RSM shows the in-plane satellite distribution corresponding to the in-plane domain patterns. **d**, Cross-sectional DF-TEM close to $[100]_{pc}$ with the $\mathbf{g} = 020_{pc}$ diffraction condition showing intensity modulations with a period of about 8.5 nm. **e**, Cross-sectional DF-TEM close to $[010]_{pc}$ with $\mathbf{g} = 002_{pc}$. See Extended Data Fig. 3 for details of the imaging conditions. The scale bars in **d** and **e** are 10 nm.

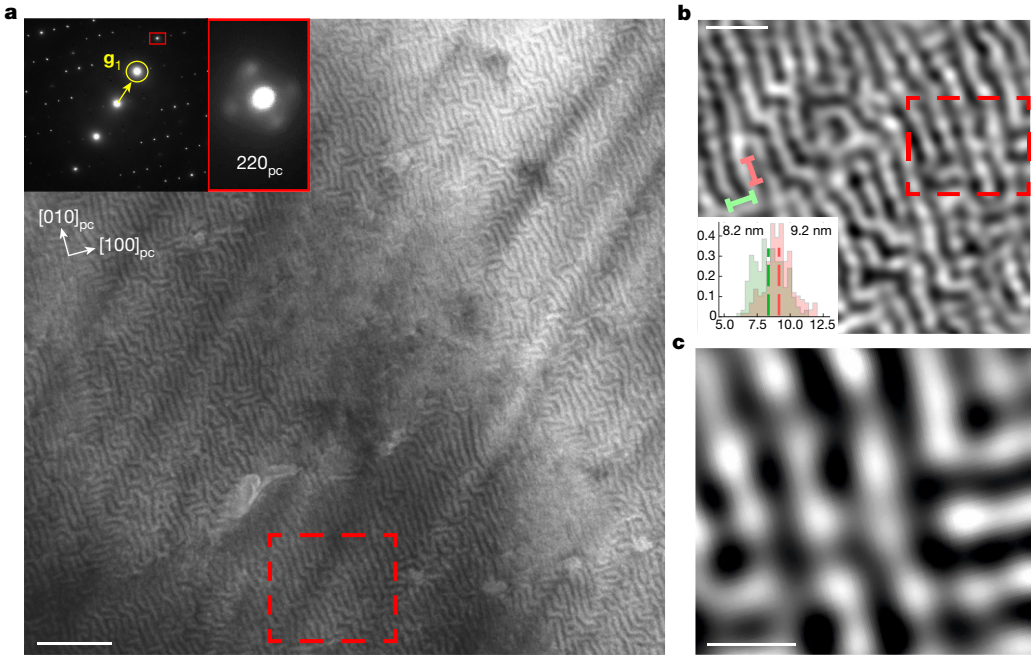

Fig. 3 | Plan-view TEM imaging. a, Plan-view DF-TEM imaging of $(SrRuO_3)_{11}/(PbTiO_3)_{13}/(SrRuO_3)_{11}$ trilayers, which shows the intricate domain pattern formed by two coexisting periodicities along $[100]_{pc}$ and $[010]_{pc}$. The inset shows the SAED pattern with the excited $\mathbf{g}_1 = 110_{pc}$ vector. Close inspection of the diffraction spots (boxed area) shows satellite decorations, similar to the X-ray data Q_x versus Q_y RSM. **b**, Noise-filtered image showing intensity modulations along the individual domains. The inset graph shows the probability distribution of finding a certain modulating period of the individual domains parallel to $[100]_{pc}$ (red) and $[010]_{pc}$ (green), respectively. **c**, Magnified area shows the locally ordered modulated domains. The scale bars are 100 nm for **a**, 30 nm for **b** and 10 nm for **c**.

$\Delta Q_y = 0.078(5)$ Å^{-1} and, hence, real-space periodicities of about 8 nm. Hints of further periodicities, also along the Q_x and Q_y directions, but with length scales of about 20–30 nm, can be seen in the tails of the central spot in the Q_x–Q_y plane (Extended Data Fig. 2c–h).

Dark-field TEM (DF-TEM) images of the same $(010)_{pc}$ and $(100)_{pc}$ cross sections were used to show the real-space arrangement of the PTO distortions (Fig. 2d, e). Periodic structures can also be observed in these TEM data along both $[010]_{pc}$ and $[100]_{pc}$ directions (Extended Data Fig. 3), with periodicities of about 8.5 nm and 7–10 nm, respectively, which are in full agreement with the periodicities determined from the X-ray data.

Therefore, regardless of the size of the investigated volume, the preparation of the sample or whether the analysis was performed in real or reciprocal space, two periodic structures with similar repeat lengths of about 8.5 nm are seen simultaneously in the $[010]_{pc}$ and $[100]_{pc}$ directions. Further analysis of these periodicities was performed using plan-view TEM imaging. Dark-field diffraction contrast and electron diffraction patterns, taken from thin sections of the TEM specimen, are shown in Fig. 3a. The $\mathbf{g}_1 = 110_{pc}$ imaging condition shows a labyrinthine domain structure[33,34] with two periodic components, running along the $[100]_{pc}$ and $[010]_{pc}$ directions. The width of the domains is about 9–10 nm and they extend for several tens of nanometres. These widths are slightly larger than those seen in the cross-sectional TEM and XRD, which is most probably because of strain relaxation when the substrate is thinned. Selected-area electron diffraction (SAED) patterns (upper-left inset of Fig. 3a) also show incommensurate satellite peaks along the $[010]_{pc}$ and $[100]_{pc}$ directions. These data are directly comparable with the macroscopic XRD data in the vicinity of the Bragg $(002)_{pc}$. The SAED patterns are highly anisotropic, with satellite peaks confined to the principal axes [h00] and [0k0], with no scattering along other in-plane directions, in agreement with the XRD. Furthermore, images taken under two beam conditions $\mathbf{g}_2 = 100_{pc}$ and $\mathbf{g}_3 = 010_{pc}$ show the two periodic structures independently (Extended Data Fig. 4b, c).

The labyrinth structure imaged under the $\mathbf{g}_1 = 110_{pc}$ excitation seems to initially consist of uniform domains oriented along $[100]_{pc}$ and $[010]_{pc}$. A bandpass filter was used to enhance the features within the domains themselves (Extended Data Figs. 5 and 6), which appear as further perturbations within the labyrinth structure, regardless of the orientation (Fig. 3b). There is a slight directional dependence of the modulating period, with periodicities of 9.2 nm and 8.2 nm along the $[010]_{pc}$ and $[100]_{pc}$ directions, respectively (inset of Fig. 3b). The juxtaposition of the labyrinth and the modulations within the domains themselves generate a local rectangular lattice of alternating contrast but, owing to the complexity of the domain pattern, ordering is only short ranged (Fig. 3c). This rectangular lattice was also reproduced within DF-TEM simulations using the Howie–Whelan equations[35], where we assume that the second modulation occurs perpendicular to the vortex-propagation direction (Extended Data Fig. 7, Supplementary Information).

So far, the results indicate that the ferroelectric domain pattern needs to be characterized by two perpendicular modulations, each described by a **Q** vector: one determining the periodicity of vortices and the other breaking the uniformity of the domains, leading to a double-**Q**-modulated state. Such incommensurate phases, triggered by several **Q** vectors, are found in magnetic materials[2,24]. For example, chiral skyrmions[3] are described by triple-**Q** cycloidal modulations. The interplay of only two orthogonal periodic modulations results in the so-called incommensurate spin crystals[11,12,26], for which the periodicities are interwoven such that they permeate all space within the magnetic material and no region can be described by one periodicity alone. The magnetic spin-crystal phases are stabilized by the non-collinear spin interactions, such as the DMi[25].

An electric DM-like interaction, which could stabilize our observed double-**Q**-modulated state, has been put forward by Zhao et al.[26]. Here the DM energy involves trilinear couplings between oxygen octahedra and atomic displacements. For bulk PTO, the atomic displacements are linked to its polar nature but there is no inherent tilting of the BO_6 octahedra. Our DFT simulations, however, show that the PTO/SRO interface causes the first layers of PTO to show pronounced in-phase

octahedra tilts in the first two unit cells, on top of the Néel winding of the dipoles, owing to the vortices themselves (Extended Data Fig. 8). Although the direction of a magnetic DM vector is dictated by the crystal symmetry[10], the components of an electric DM vector depend on the axes around which the oxygen cage is rotated[26]. Oxygen octahedral tilt propagation from the SRO into the PTO could enable the oxygen octahedra rotations to couple to the Néel character of the surface dipoles, resulting in DM-like interactions as a source of the second modulation we observe. This interface-induced effect would be analogous to the DMi induced by interfacial symmetry breaking in ferromagnets[13,36,37].

On the basis of the TEM and XRD data presented above, we consider that the ferroelectric polarization orders itself in a domain pattern similar to the magnetic incommensurate spin crystal phases given by two perpendicular periodicities, namely, the incommensurate spin crystal 1 (SC1)[38]. Although it is very clear that the observed structure has two coexisting modulation vectors, a complete model of the variation of polarization and strain in three dimensions still remains to be determined, because we can only observe periodicities using diffraction and a projection of the structure using transmission microscopy. The plan-view TEM data indicate that the weaker modulation produces periodic displacements that are parallel to the vortex core, but it remains to be determined whether this occurs by cycloidal modulations, such as $\mathbf{Q}_c = C_c \sin(qx)\,\mathbf{e}_{[100]} + C_c \cos(qx)\,\mathbf{e}_{[001]}$ (with x defined as the $\mathbf{e}_{[100]}$ coordinate component of the position vector), or some other—more complicated—interactions. For example, using our DFT simulations to build a 3D vortex array (Fig. 4a), we obtain identical plan-view projections by adding a helical modulation, given by $\mathbf{Q}_h = C_h \sin(qx)\mathbf{e}_{[010]} + C_h \cos(qx)\,\mathbf{e}_{[001]}$ (Fig. 4b) or cycloidal modulation (Fig. 4c). Projections of the 3D polarization model into the $[001]_{pc}$–$[010]_{pc}$ and $[010]_{pc}$–$[100]_{pc}$ planes show that both modulations preserve the vortex pattern in the cross-sectional $[001]_{pc}$–$[010]_{pc}$ plane (Extended Data Fig. 9), but only the cycloidal model reproduces the expected atomic displacements in both the $[001]_{pc}$–$[010]_{pc}$ and the $[010]_{pc}$–$[100]_{pc}$ planes.

Further evidence supporting the cycloidal-like interaction can be extracted from X-ray circular dichroism (CD) experiments. We used non-resonant scattering and investigated the 2D topologies with the sample orientated such that either the $[100]_{pc}$ // $[001]_o$ or the $[010]_{pc}$ // $[-110]_o$ direction was in the scattering plane (see Extended Data Fig. 10a, b). Measurement of the CD under rotation of the sample by 180° shows a weak dichroic signal when the $[100]_{pc}$ direction is in the scattering plane, but—crucially—no dichroic signal on rotating the sample by 90° (see Extended Data Fig. 10c, d). We therefore conclude that the interaction potential giving rise to the second modulation does not contain terms in $\mathbf{Q}$ proportional to $\mathbf{e}_{[010]}$, thereby suggesting that the interaction is cycloidal.

In summary, we have shown that ordered arrays of topological features such as polar vortices also form in a ferroelectric environment, even where the depolarization field is reduced by the choice of metallic SRO electrodes. Moreover, the ferroelectric polarization generates a new ordered phase described by a double-$\mathbf{Q}$ modulation that combines a vortex state with a sinusoidal modulation. Although TEM and XRD cannot distinguish between the helical and cycloidal modulations, DFT and dichroism point towards a cycloidal double-$\mathbf{Q}$ structure. Such a topology mimics, in detail, the incommensurate spin crystal phase SC1 recently found in magnetic materials. The presence of such a double-$\mathbf{Q}$ structure would require an electric counterpart of the magnetic DMi, which has been suggested by Zhao et al.[26]. Such an electric DMi could provide the phenomenological explanation of the emergence of magnetic-like phases in ferroelectric systems. Given the similarity to the magnetic spin crystals, we chose here the simplest model to explain the data. However, we cannot rule out alternative, more complex topologies that would yield similar double-$\mathbf{Q}$ structures. Further advanced modelling and simulation would be necessary to identify the exact polarization pattern such complex interactions would produce and which advanced experimental methods will be needed to uniquely evidence it.

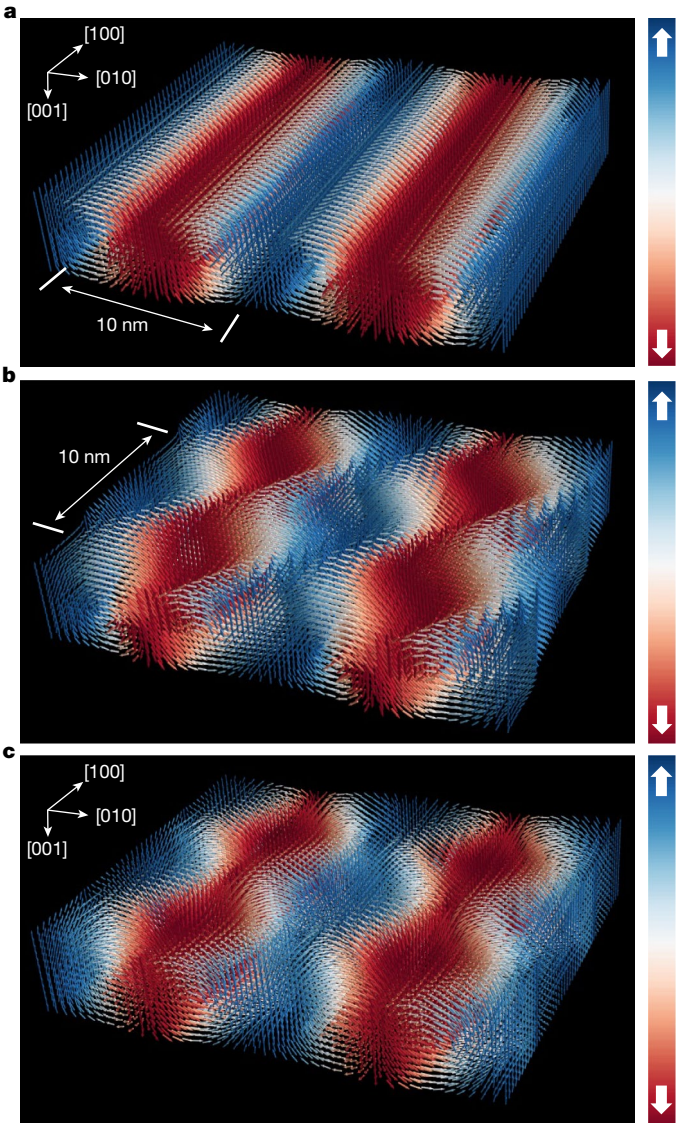

Fig. 4 | Double modulation. a, Pseudo 3D representation showing plan and front views through regular polar vortices. **b**, Vortex arrays with a second helical modulation along the vortex core. **c**, Vortex arrays with a second cycloidal modulation along the vortex core. The colour bar maps the projection of the dipole along [001]: white regions contain dipoles oriented parallel to [010], whereas red and blue regions describe dipoles oriented parallel (red) and antiparallel (blue) to [001].

Our findings provide a potential pathway for technological exploitation and a fertile framework for further fundamental studies exploring physical phenomena. Such studies would pave the way for the exploration of complex ferroelectric topologies triggered by the electric DMi, similar to topological spin textures found in ferromagnets. Along with the discovery of polar vortices and skyrmions, our findings further blur the border between emergent ferromagnetic and ferroelectric dipole topologies. Understanding of the fundamental similarities between the manifestation of spin textures across multiferroics is still lacking; however, our findings provide further evidence for the potential of the ferroelectric systems to mimic their magnetic counterparts. Complex topological structures are not native to magnetism, presenting themselves throughout the sciences[39,40]. The understanding gained from investigations of the fundamental mechanisms within multiferroics extends far beyond applications in condensed-matter physics.

Online content

Any methods, additional references, Nature Research reporting summaries, source data, extended data, supplementary information, acknowledgements, peer review information; details of author contributions and competing interests; and statements of data and code availability are available at https://doi.org/10.1038/s41586-021-04260-1.

1. Wachowiak, A. et al. Direct observation of internal spin structure of magnetic vortex cores. *Science* **298**, 577–580 (2002).
2. Seki, S., Yu, X. Z., Ishiwata, S. & Tokura, Y. Observation of skyrmions in a multiferroic material. *Science* **336**, 198–201 (2012).
3. Yu, X. Z. et al. Real-space observation of a two-dimensional skyrmion crystal. *Nature* **465**, 901–904 (2010).
4. Yadav, A. K. et al. Observation of polar vortices in oxide superlattices. *Nature* **530**, 198–201 (2016).
5. Hsu, S.-L. et al. Emergence of the vortex state in confined ferroelectric heterostructures. *Adv. Mater.* **31**, 1901014–1901022 (2019).
6. Shafer, P. et al. Emergent chirality in the electric polarization texture of titanate superlattices. *Proc. Natl Acad. Sci. USA* **115**, 915–920 (2018).
7. Gruverman, A. et al. Vortex ferroelectric domains. *J. Phys. Condens. Matter* **20**, 4 (2008).
8. Nelson, C. T. et al. Spontaneous vortex nanodomain arrays at ferroelectric heterointerfaces. *Nano Lett.* **11**, 828–834 (2011).
9. Dzyaloshinsky, I. Thermodynamic theory of weak ferromagnetism of antiferromagnetics. *J. Phys. Chem. Solids* **4**, 241–255 (1958).
10. Moriya, T. Anisotropic superexchange interaction and weak ferromagnetism. *Phys. Rev.* **120**, 91–98 (1960).
11. Kurumaji, T. et al. Néel-type skyrmion lattice in the tetragonal polar magnet $VOSe_2O_5$. *Phys. Rev. Lett.* **119**, 237201–237205 (2017).
12. Kurumaji, T. et al. Direct observation of cycloidal spin modulation and field-induced transition in Néel-type skyrmion-hosting $VOSe_2O_5$. *J. Phys. Soc. Jpn* **90**, 024705 (2021).
13. Seddon, S. D. et al. Real-space observation of ferroelectrically induced magnetic spin crystal in $SrRuO_3$. *Nat. Commun.* **12**, 2007 (2021).
14. Hong, Z. et al. Stability of polar vortex lattice in ferroelectric superlattices. *Nano Lett.* **17**, 2246–2252 (2017).
15. Damodaran, A. R. et al. Phase coexistence and electric-field control of toroidal order in oxide superlattices. *Nat. Mater.* **16**, 1003–1009 (2017).
16. Stoica, V. A. et al. Optical creation of a supercrystal with three-dimensional nanoscale periodicity. *Nat. Mater.* **18**, 377–383 (2019).
17. Li, X. et al. Atomic-scale observations of electrical and mechanical manipulation of topological polar flux closure. *Proc. Natl Acad. Sci. USA* **117**, 18954–18961 (2020).
18. Ponomareva, I., Naumov, I. I. & Bellaiche, L. Low-dimensional ferroelectrics under different electrical and mechanical boundary conditions: atomistic simulations. *Phys. Rev. B* **72**, 214118 (2005).
19. Sanchez-Santolino, G. et al. Resonant electron tunnelling assisted by charged domain walls in multiferroic tunnel junctions. *Nat. Nanotechnol.* **12**, 655–662 (2017).
20. Penthorn, N. E., Hao, X., Wang, Z., Hua, Y. & Jiang, H. W. Experimental observation of single skyrmion signatures in a magnetic tunnel junction. *Phys. Rev. Lett.* **122**, 257201 (2019).
21. Peters, J. J. P., Apachitei, G., Beanland, R., Alexe, M. & Sanchez, A. M. Polarization curling and flux closures in multiferroic tunnel junctions. *Nat. Commun.* **7**, 13484 (2016).
22. Hadjimichael, M. et al. Metal–ferroelectric supercrystals with periodically curved metallic layers. *Nat. Mater.* **20**, 495–502 (2021).
23. Li, S. et al. Periodic arrays of flux-closure domains in ferroelectric thin films with oxide electrodes. *Appl. Phys. Lett.* **111**, 052901 (2017).
24. Kurumaji, T. et al. Skyrmion lattice with a giant topological Hall effect in a frustrated triangular-lattice magnet. *Science* **365**, 914–918 (2019).
25. Yi, S. D., Onoda, S., Nagaosa, N. & Han, J. H. Skyrmions and anomalous Hall effect in a Dzyaloshinskii-Moriya spiral magnet. *Phys. Rev. B* **80**, 054416–054421 (2009).
26. Zhao, H. J., Chen, P., Prosandeev, S., Artyukhin, S. & Bellaiche, L. Dzyaloshinskii–Moriya-like interaction in ferroelectrics and antiferroelectrics. *Nat. Mater.* **20**, 341–345 (2021).
27. Aguado-Puente, P. & Junquera, J. Ferromagnetic-like closure domains in ferroelectric ultrathin films: first-principles simulations. *Phys. Rev. Lett.* **100**, 177601–177604 (2008).
28. Dürr, H. A. et al. Chiral magnetic domain structures in ultrathin FePd films. *Science* **284**, 2166–2168 (1999).
29. Ahn, C. H. et al. Ferroelectric field effect in ultrathin $SrRuO_3$ films. *Appl. Phys. Lett.* **70**, 206–208 (1997).
30. Jia, C.-L. et al. Atomic-scale study of electric dipoles near charged and uncharged domain walls in ferroelectric films. *Nat. Mater.* **7**, 57–61 (2008).
31. Naumov, I., Bellaiche, L. & Fu, H. Unusual phase transitions in ferroelectric nanodisks and nanorods. *Nature* **432**, 737–740 (2004).
32. Junquera, J. & Ghosez, P. Critical thickness for ferroelectricity in perovskite ultrathin films. *Nature* **422**, 506–509 (2003).
33. Nahas, Y. et al. Topology and control of self-assembled domain patterns in low-dimensional ferroelectrics. *Nat. Commun.* **11**, 5779 (2020).
34. Nahas, Y. et al. Inverse transition of labyrinthine domain patterns in ferroelectric thin films. *Nature* **577**, 47–51 (2020).
35. Carter, C. B. & Williams, D. B. *Transmission Electron Microscopy: Diffraction, Imaging, and Spectrometry* (Springer, 2016).
36. Bode, M. et al. Chiral magnetic order at surfaces driven by inversion asymmetry. *Nature* **447**, 190–193 (2007).
37. Udalov, O. G., Beloborodov, I. S. & Sapozhnikov, M. V. Magnetic skyrmions and bimerons in films with anisotropic interfacial Dzyaloshinskii-Moriya interaction. *Phys. Rev. B* **103**, 174416 (2021).
38. Chen, J., Zhang, D. W. & Liu, J. M. Exotic skyrmion crystals in chiral magnets with compass anisotropy. *Sci. Rep.* **6**, 29126 (2016).
39. Saw, T. B. et al. Topological defects in epithelia govern cell death and extrusion. *Nature* **544**, 212–216 (2017).
40. Tsesses, S. et al. Optical skyrmion lattice in evanescent electromagnetic fields. *Science* **361**, 993–996 (2018).

Methods

DFT simulations

The calculations were performed using the Quantum ESPRESSO suite[41,42] plane-wave code with the generalized gradient approximation. The exchange-correlation functional is in the Perdew–Burke–Ernzerhof parameterization[43], adapted for solids, PBEsol. We used Vanderbilt ultrasoft pseudopotentials with elements having their valence states composed of: Pb 5*d*10 6*s*2 6*p*2, Sr 4*s*2 4*p*6 4*d*1 5*s*1 5*p*0, Ti 3*s*2 3*p*6 4*s*2 3*d*2, Ru 4*d*7 5*s*1 5*p*0 and O 2*s*2 2*p*4. The integration of the Brillouin zone is performed over an automatically generated Monkhorst–Pack[44] *k*-mesh with a Gaussian smearing of 0.01 eV. The kinetic energy cut-off is 70 Ry and 450 Ry for the charge density.

All systems have 6.5 unit cells of SRO and 5.5 unit cells of PTO (along the *z* axis). To allow the polarization to form domains, we built a supercell with one unit cell along the *y* axis, $N_y = 1$, and ten unit cells along the *x* axis, $N_x = 10$. Here the *z* axis is out of plane and the *x* and *y* axes are orthogonal in-plane directions. The in-plane lattice constant is set equal to DSO, which, in the pseudocubic setting, is 3.953 Å. Atomic relaxations of bulk PTO and SRO were carried out under the strain imposed by the substrate, with the resulting unit cells used to construct the supercell. Using the PBEsol functional, the relaxed unstrained bulk PTO unit cell yields lattice constants equal to $a = 3.873(1)$ and $c = 4.218$(A), resulting in a c/a ratio of 1.089 (that is, within 1.7% error of the experimental value[45]). The SRO thickness was chosen such that the PTO layer was decoupled from its periodic images[46].

Spin–orbit coupling is very weak for PTO and was not considered. Hubbard corrections were not used. The supercell forces converged to less than 80 meV $Å^{-1}$ per atom (600 atoms).

Materials

We used lead titanate (PTO), strontium titanate (STO), strontium ruthenate (SRO) and dysprosium scandate (DSO). DSO is a band insulator[47] with an orthorhombic unit cell belonging to the *Pbnm* space group with lattice parameters equal to $a = 5.4494$ Å, $b = 5.7263$ Å and $c = 7.9132$ Å. STO is a band insulator[48] with a cubic unit cell with a lattice constant $a = 3.905$ Å and space group $Pm\bar{3}m$. SRO is a metal[49] at room temperature with a crystal symmetry that belongs to the orthorhombic Bravais lattice described by the *Pbnm* space group and lattice parameters $a = 5.5684$ Å, $b = 7.8425$ Å and $c = 5.532$ Å. PTO is a ferroelectric with a Curie temperature of 490 °C and has a tetragonal unit cell[50] described by the *P4mm* space group with $a = 3.904$ Å and $c = 4.178$ Å.

Film growth by pulsed laser deposition

DSO $(110)_o$-oriented substrates with a miscut angle of <0.05° were prepared by thermal annealing at 1,030 °C for 2 h in an oxygen-rich atmosphere. Epitaxial SRO/PTO/SRO film structures were deposited onto the STO-buffered DSO $(110)_o$ substrates using reflective, high-energy, electron-diffraction-assisted pulsed laser deposition, which enabled precise control of the layer thickness. The thickness, growth temperature and laser fluence for STO/SRO/PTO/SRO are 10/11/13/11 unit cells, 600/670/600/600 °C and around 1/0.8/1/0.8 J cm^{-2}, respectively. The laser repetition rate was 3 Hz for all layers, at 0.1 mbar oxygen pressure. The cooling rate was 20 °C min^{-1} in 200 mbar of O_2. The PTO target is an in-house compressed and sintered pellet with 10% lead excess to compensate for the high lead volatility during growth at 600 °C.

X-ray studies

Diffraction studies were carried out at the I16 beamline of the Diamond Light Source using energy 8.04 keV and a spot size of 200 μm × 60 μm (h × v). The sample was mounted on the six-circle kappa goniometer with a Pilatus 100K Area Detector and orientated using the substrate. For simplicity, we refer to the planes and directions in the pseudo-cubic setting, which have the following epitaxial relationships: $[110]_o = [001]_{pc}$; $[001]_o = [100]_{pc}$; $[-110]_o = [010]_{pc}$. Dichroism experiments were performed at 7.7 keV on beamline 4-ID-D at the Advanced Photon Source, Argonne National Laboratory, with the circular polarized light generated using a diamond phase retarder. Lab-based XRD studies were also performed using a PANalytical X'Pert Pro MRD diffractometer with Cu K_α radiation and an 1D PIXcel detector.

Sample preparation for electron microscopy studies

STEM and cross-sectional DF-TEM samples were prepared using the TESCAN FIB-SEM system. The sample was flat polished, starting with an ion energy of 30 keV, before decreasing to 2 keV for the final polish. Plan-view DF-TEM samples were flat polished on an Allied High Tech MultiPrep to 30 μm, followed by further thinning in a Gatan Precision Ion Polishing System with starting energy 6 keV, which decreased to 100 eV for final cleaning. STEM images were recorded in a double-CEOS-corrected Schottky emission JEOL ARM200F microscope operating at 200 kV. Annular dark-field (ADF) signals were collected in the range 45–180 mrad, with a probe forming a convergence semi-angle of 21 mrad. For accurate position/displacement measurements, each image is reconstructed from several orthogonal fast scans, which were aligned for rigid and non-rigid distortions using the SmartAlign routines[51]. Atomic positions were then found using nonlinear least squares fitting of 2D Gaussian functions including contributions from nearest neighbours. Diffraction contrast images were recorded with two-beam conditions on a JEOL 2100 transmission electron microscope with a LaB_6 filament operating at 200 kV.

Diffraction contrast simulations

Contrast in dark-field TEM images is primarily produced by the internal strain field of the vortex structures. Some insight into these strain fields can be obtained by choosing different **g** vectors, as the only components that contribute to contrast are parallel to **g**. A simple two-beam Howie–Whelan simulation reproduces the essential features of the image (Extended Data Fig. 7). A vortex, with displacements perpendicular to its line direction **u**, appears as a line of contrast perpendicular to **g** and becomes invisible when **g** is parallel to **u**. The coexistence of two modulations is therefore confirmed by the dark-field $\mathbf{g} = 100_{pc}$ and $\mathbf{g} = 010_{pc}$ images, which show continuity of structures in both directions.

Film structure characterization

The surface of the films resulting from pulsed laser deposition were studied using AFM, which showed atomically flat layers, as seen in Extended Data Fig. 1a. The vicinal structure, imposed by the substrate miscut angle (~0.003°), is retained through all the component layers. The vertical step between adjacent terraces is about 4 Å (1 unit cell) and the roughness of each terrace is below 1 Å.

A low-magnification, cross-sectional STEM image of the sample is shown in Extended Data Fig. 1b. The STEM data show the well-defined and smooth layers, with layer thicknesses as expected from the nominal structure.

Reciprocal space mapping

The sample was aligned on all instruments with the Q_x, Q_y and Q_z directions coincident with the $[h00]_{pc}$, $[0k0]_{pc}$ and $[00l]_{pc}$ crystallographic directions. Scattering from volumes of reciprocal space were recorded in the vicinity of the 002_{pc} and 103_{pc} reciprocal lattice points and are presented in Extended Data Fig. 2a, b, respectively, with the 103_{pc} data recorded on a laboratory source and the 002_{pc} data on I16 at Diamond Light Source.

Crystal truncation rods (CTRs) around the substrate peaks contain the collective reflections from all the layers. Around both the symmetric $(002)_{pc}$ and the asymmetric $(103)_{pc}$ reflections, the CTRs are found at the same in-plane **Q** as the substrate peak, showing that all layers are fully strained to the substrate, with identical in-plane lattice constants for all the layers.

To extract the real-space periodicities from the location of satellite peaks, the 3D scattering volume was first collapsed into 2D maps by integrating along the third reciprocal direction to produce Q_z–Q_x, Q_z–Q_y and Q_x–Q_y RSMs (Extended Data Fig. 2a). Then, we plot the intensity distribution along the relevant directions as shown in Extended Data Fig. 2c–h.

We start by considering the collapsed Q_z–Q_x full RSM (Extended Data Fig. 2c), which contains the surface CTRs at $Q_x = 0$ and streaks of intensity centred on $Q_x = \pm 0.07$ Å^{-1} arising from the periodic structure. Extracted 1D Q_z scans determined at $Q_x = 0$ and the first-order satellite peak ($Q_x = 0.07$ Å^{-1}) are shown in Extended Data Fig. 2d. The surface CTRs are dominated by the substrate reflection at $Q_z = 3.119$ Å^{-1} but the layer peaks can be seen as shoulders at $Q_z = 3.108(2)$ Å^{-1} and $Q_z = 3.224(2)$ Å^{-1}. The extracted CTRs recorded at the satellite reflection scan show two peaks: the first—and most intense peak—is centred at 3.108(2) Å, with the second centred at the first-order interference fringe. The zero-order peak shows that the periodic structures are contained in a layer that has an out-of-plane lattice constant of about 4.05(2) Å. The width of the peak is broad and about 0.120(5) Å^{-1} and is a direct measure of the layer thickness from which the satellite originates. In this case, this corresponds to a layer that is 5.25(15) nm thick. Both the average out-of-plane lattice constant and the layer thickness indicate that the host layer to the diffraction satellites is the ferroelectric PTO layer.

More detailed analysis of the periodic functions along the $[100]_{pc}$ direction can be obtained by considering extracted scans in Q_x. To improve the signal-to-noise ratio, the Q_x line scans shown in Extended Data Fig. 2e were calculated by integrating a region of Q_z, as shown by the highlighted box in Extended Data Fig. 2c. The resulting 1D plot of the diffraction intensity along the Q_x direction shows the first-order and second-order satellite peaks and their widths, as seen in Extended Data Fig. 2e. The extent of the long-range order can be obtained from the width of the satellite peaks. Along the Q_x ($[100]_{pc}$) direction, we estimate the domains to have a coherent length of approximately 45 nm. However, as the second-order satellites have a width roughly twice that of the first-order satellites, there must also be some dispersion in the periodicity leading to further peak broadening. There are also indications of further periodicities in the tails of the central Bragg peak around 0.02 Å^{-1}, corresponding to a periodicity of 30 nm.

Exploring the periodicities along the $[010]_{pc}$ direction follows a similar process, but—this time—initially integrating the intensity in Q_x to produce a Q_z–Q_y RSM (Extended Data Fig. 2f) before extracting a cut in Q_y by integrating Q_z, shown in Extended Data Fig. 2g. This cut in reciprocal space shows broad satellite peaks with a spacing of about $\Delta Q_y = 0.078(5)$ Å^{-1} and periodicities of approximately 8 nm. Second-order satellites are absent, indicating that—along this direction—they are less well ordered than in Q_x. Nevertheless, the full width at half maximum of the satellite peaks is 0.03 Å^{-1}, showing a coherent length of about 20 nm in the Q_y direction. As in the Q_x scan, hints of further periodicities can be seen in the tails of the central peak at reciprocal space values of 0.022(5) Å^{-1}, corresponding to features with periodicities in the 22–28-nm range.

The diffraction from the periodic array is more easily seen in a Q_x–Q_y RSM, in which the data collapse has been achieved by integrating the intensity along Q_z (Extended Data Fig. 2h). In all projections, we observe periodicities of about 8–8.5 nm along the principal [h00] and [0k0] axes, with a spatial extension of about 45 nm and about 25 nm, respectively, along with further short-ranged periodic features of about 22–28 nm coexisting in the sample.

DF-TEM analysis

Whereas XRD studies show features originating from periodic perturbations localized within the PTO layer, this technique cannot provide clear real-space information about the local atomic displacements and, hence, the polarization distribution. To obtain more information about the local structure, we use DF-TEM to visualize and analyse these lattice perturbations. In Extended Data Fig. 3a, b, we show dark-field images of a $(100)_{pc}$ cross-section specimen under $\mathbf{g} = 020_{pc}$ and $\mathbf{g} = 002_{pc}$ excitation conditions. Under the $\mathbf{g} = 020_{pc}$ excitation, the dark-field contrast shows a sinusoidal pattern along $[010]_{pc}$, which is produced by a modulation of the in-plane component of the internal strain field (and, hence, polarization). Furthermore, under the $\mathbf{g} = 002_{pc}$ condition, we see that the dark-field contrast shows features of alternating bright/dark regions, corresponding to a modulation of the out-of-plane component of the internal strain fields. These characteristics are consistent with those found in PTO/STO superlattices, which show pairs of clockwise–anticlockwise vortices[52]. Along the perpendicular $[100]_{pc}$ direction (Extended Data Fig. 3c), the diffraction contrast ($\mathbf{g} = 002$) shows short-ranged periodic features, with periodicities that match the XRD data.

To study how the two cross-sectional periodicities are interwoven, plan-view dark-field studies were performed on samples with most of the substrate milled away to allow the sample to be electron transparent. Extended Data Figure 4a shows a low-magnification image of the periodic structures under $\mathbf{g}_1 = 110_{pc}$. A labyrinth pattern is observed that comprises interwoven domains that run along the principal axes $[100]_{pc}$ (Q_x) and $[010]_{pc}$ (Q_y), with periodicities of about 9–10 nm. The slight discrepancy between X-ray and TEM periodicities probably arises from strain relaxation because of having milled away most of the substrate. Nevertheless, from the X-ray analysis, we determined that the periodic structures (periodicities of about 9–10 nm) along Q_x and Q_y have a coherent length of about 45 nm and 22–28 nm, respectively. The plan-view DF-TEM shows the real-space domain pattern, and these values are shown to relate to the average length of the individual domains running along the $[010]_{pc}$ and $[100]_{pc}$ directions (inset of Extended Data Fig. 4a).

Conveniently, the $\mathbf{g}_2$ vector can be decomposed into orthogonal components, $\mathbf{g}_2 = 100_{pc}$ and $\mathbf{g}_3 = 010_{pc}$, which highlight the two modulations independently (Extended Data Fig. 4b, c). Plan-view dark-field images taken under $\mathbf{g}_2$ and $\mathbf{g}_3$ excitation vectors show periodic structures of about 10 nm perpendicular to the excitation vector. The periodic character is reflected by satellite decorations around diffraction peaks, as seen in the inset of Extended Data Fig. 4b, c.

To improve the signal-to-noise ratio, a bandpass filter was used on the 2D Fourier transform. This way, we impose a frequency cut-off for the random high-frequency signal that is related to the noise in the system. Ultimately, we allow for frequencies of $0.015 < |\mathbf{Q}| < 0.16$ nm^{-1}, which correspond to real-space periodicities of $67 > |\mathbf{R}| > 6.3$ nm. This enables periodicities within this interval to manifest in the real-space image. The 2D Fourier transforms show that all Fourier satellites are well within the bandpass filter. As seen in the succession of images from Extended Data Fig. 5a–c, the bandpass filter cleans the data showing intensity modulation along the individual domains.

Line profiles along the brighter contrast pattern (Extended Data Fig. 6a) and darker contrast structures (Extended Data Fig. 6b) show periodic intensity modulations in both unfiltered and filtered data. Such intensity modulations are present regardless of the local structure and have the same periodicity in both the filtered and the unfiltered data. This shows the effectiveness of the bandpass filter used to clean the signal and provides further evidence that the filtering process does not induce further artefacts but only removes the high-frequency noise.

Two-beam diffraction contrast simulations

To give some indication of the probable contrast of an array of vortices in DF-TEM, we performed diffraction contrast simulations within the two-beam Howie–Whelan formalism. Although this does not reproduce contrast in images taken with a large deviation from the Bragg condition—that is, weak-beam dark-field images—it gives an indication of the strength of the contrast and its sensitivity to different choices of diffraction vector. We simulate a 2D array of perfect vortices with displacement

R, given by $R = Ad^n\exp(-\alpha d^n)$, where d is the distance from the vortex core, with parameters $n = 1.15$ and $\alpha = 0.6$ chosen to match those observed in our cross-section atomic-resolution ADF-STEM images.

As shown in Extended Data Fig. 7, the simulated contrast of a vortex array is a reasonable match with experimental images in that a vortex appears as a single line of contrast that lies perpendicular to the diffraction vector. Experimentally, we observe vortex arrays visible in both $\mathbf{g} = 100_{pc}$ and $\mathbf{g} = 010_{pc}$ directions, but those running along $[100]_{pc}$ give weaker contrast than those running along $[010]_{pc}$. We therefore choose the magnitude of the displacement as $A = 0.03$ for vortices along $[010]_{pc}$ and $A = 0.003$ for vortices along $[100]_{pc}$. This gives a modulated contrast in a Fourier-filtered $\mathbf{g} = 110_{pc}$ image that is a reasonable match with experiment. The simulations were performed using an in-house script that can be found on GitHub (https://github.com/WarwickMicroscopy/Howie-Whelan_Polarisation-vortex). For further details about the simulations, see the Supplementary Information.

PTO/SRO interface (DFT)–oxygen cage tilt analysis

The property that no region of space within the ferroelectric can be described by one periodicity alone can be inferred from the X-ray RSM and the TEM plan-view dark-field contrast data. Whereas this characteristic has not been observed in ferroelectrics, it is uniquely found in DM-stabilized magnetic domain topologies. The similarity between these topologies raises the question whether these structures are mediated by an interaction that is similar in form to the magnetic DM coupling. In a recent publication, Zhao et al.[26] have put forward the possibility of specific couplings that can result in non-zero DM-like energies. Such couplings have the form of trilinear products between oxygen octahedra tilts and nearest-neighbour displacements. In PTO, the displacement direction of the B-site relative to its oxygen cage indicates the direction of the polarization[30] and allows the two to be fundamentally linked.

Polar vortices are not unique to PTO/SRO trilayers and they can be readily observed in STO/PTO/STO structures[5] as a result of the interplay between strain, gradient and electric energies. Unlike STO, SRO is a material that shows oxygen octahedra rotation[49]. Earlier works have shown that tilted structures can induce tilts in non-tilted structures through the interface proximity[53–56].

Such behaviour is reproduced in our DFT supercell, as seen in Extended Data Fig. 8. At the interface with SRO, the PTO shows pronounced in-phase octahedra tilts localized to the first two unit cells, on top of the Neel winding of the dipoles because of the vortices themselves. Although the supercell does not allow for tilts along all three directions, one could argue that the interface of PTO will undergo even more complex structural distortions, with oxygen tilts along all three axes[57], which are shown to couple to the polar distortions[58].This mechanism is triggered by the interface, in a manner similar to the interfacial DMi in magnets[13,36].

Model–experiment comparison

In the cross-sectional STEM, the recorded image necessarily shows the projection of all the atoms within the volume that interact with the electron beam. Considering that all the layers (STO, SRO and PTO) have a pseudo-cubic crystal symmetry, the sample is aligned in such a way that the main crystallographic axes $[100]_{pc}$ and $[010]_{pc}$ are parallel to the electron beam. As a result, the displacement maps show an average of the spatial distortion throughout the sampling volume (that is, the thickness of the sample that the columns of atoms—parallel to the beam—are subjected to).

On the basis of the XRD and the TEM data, we have built 3D polarization models that consider a double-**Q** modulation of the polarization vector field. One **Q** vector is associated with the vortex ordering and the second describes the modulation along the vortices, which is either cycloidal, $\mathbf{Q}_c = C_c \sin(qx)\,\mathbf{e}_{[100]} + C_c \cos(qx)\,\mathbf{e}_{[001]}$, or helical, $\mathbf{Q}_h = C_h \sin(qx)\mathbf{e}_{[010]} + C_h \cos(qx)\,\mathbf{e}_{[001]}$, where x is the $\mathbf{e}_{[100]}$ coordinate component of the position vector. To check the validity of our models, we compare the projected polarization pattern along both $[100]_{pc}$ and $[010]_{pc}$ directions with the experimental STEM polarization maps. The projection is achieved by averaging the polar vectors along the viewing direction. On the basis of the XRD data, we know that there are two coexisting orthogonal periodicities, with different strengths. With respect to this, one modulation is set to strength one and the helical-like/cycloidal-like modulation has C_h and C_v set to 0.7. The value of q is set to one and it is used only to have a dimensionless qx product.

Extended Data Figure 9a, b show the atomic displacements when viewed along the $[100]_{pc}$ and $[010]_{pc}$ directions. Experimental data (top row) are compared with projections of 3D theoretical calculations from possible topologies onto the same axis. The helical and cycloidal modulated vortex models show that the vortex structure is retained along the $[010]_{pc}$ direction. Along the $[100]_{pc}$ direction, however, the experimental data show that the displacements throughout the thickness of the PTO is mostly confined into either up or down domains. Nevertheless, some areas within the layer show that the displacements—and hence polarization—rotate continuously between these domains. This behaviour is reproduced only by the cycloidal modulated vortices and is not found for the helical-like modulation, as it does not allow for in-plane rotation of the polarization vector. An alternative model where the second modulation is given by a second array of ideal vortices perpendicular to the first would produce atomic displacements with vortices along both the $[100]_{pc}$ and the $[010]_{pc}$ directions, and is not observed experimentally.

These results provide evidence that the periodic intensity oscillations along the domains shown in Extended Data Figs. 4–6 will probably emerge from an ordered array of polar vortices modulated by a second **Q** vector characterized by a cycloidal displacement pattern.

X-ray dichroism experiment

Information about possible helicities within the 2D array can be extracted from a non-resonant study of the samples using circularly polarized photons. The sample was orientated such that the $[100]_{pc}$// $[001]_o$ direction is in the scattering plane and along the beam direction at the azimuthal angle 0°. Experiments were performed at four azimuthal angles, 0°, 90°, 180° and 270°. At each azimuth, rocking curves within the scattering plane were used to measure the satellite reflections along the H and K directions. Our experimental results are shown in Extended Data Fig. 10a, b. At each point in the scan, the intensity was recorded separately for each beam helicity and for fixed monitor count. The resulting 'sum' signal is obtained by averaging the measured intensities for the two helicities and the CD determined from the difference signal, normalized to the sum signal. The sum data in Extended Data Fig. 10a, b are fully consistent with the XRD studies reported previously, with the satellite reflections stronger when the $[100]_{pc}$ //$[001]_o$ direction is in the scattering plane.

The measured CD signal contains a mix of components that can be separated by recording the CD intensity at two azimuthal angles separated by 180° and looking at either the difference or the sum of the recorded CD intensities. This generates a second pair of dichroic signals: either $(CD_0 \pm CD_{180})/2$ or $(CD_{90} \pm CD_{270})/2$, depending on which crystallographic direction is being analysed. The $(CD_0 - CD_{180})/2$ or $(CD_{90} - CD_{270})/2$ data yield information on any time-reversal symmetry-breaking terms. In the third panel of Extended Data Fig. 10, we show this extra dichroic signal, demonstrating a symmetry-breaking signal along the $[100]_{pc}$ direction and highlight that it has the same sign and magnitude when measured at either the +1 or the −1 satellite position.

In Extended Data Fig. 10c, d, we present the processed results of the CD data. As the data from the two satellites are in excellent agreement, we can consolidate the data and reduce the uncertainties. We first focus on the dichroic signals ($(CD_0 - CD_{180})/2$ and $(CD_{90} - CD_{270})/2$). When the sample is orientated with $[100]_{pc}$ in the scattering plane,

we see a (weak) dichroic signal, which disappears on rotation of the sample by 90° when the $[010]_{pc}$ direction is in the scattering plane. The lack of a dichroic signal in the $[010]_{pc}$ direction is either the result of no symmetry-breaking terms or two terms of equal but opposite sign that cancel completely.

By contrast, the $(CD_0 + CD_{180})/2$ and $(CD_{90} + CD_{270})/2$ signals are remarkably consistent for the two sample orientations. As the measured linear polarization content was very small, we rule out the signal as arising from linear dichroism or a simple polarization factor. One possible explanation is that this signal originates from natural CD from the underlying birefringence of the material, which is invariant under sample reversal.

The data show that there must exist a strain modulation along the $[100]_{pc}$ direction that breaks time-reversal symmetry as the sample is rotated by 180°. Of the two proposed mechanisms for the second modulation, it is only the cycloidal modulation of the form $\mathbf{Q}_c = C_c \sin(qx)\,\mathbf{e}_{[100]} + C_c \cos(qx)\,\mathbf{e}_{[001]}$ that has the correct propagation vector and symmetry required. The observed CD data are consistent with the $(CD_0 - CD_{180})/2$ dichroic signal originating from a small scattering volume and support the overarching hypothesis that the second modulation might be driven by an electric DMi that is localized at the interfaces.

Data availability

The data that support the findings of this study are available at the University of Warwick open access research repository (http://wrap.warwick.ac.uk/159776/) or from the corresponding author on reasonable request.

41. Giannozzi, P. et al. Advanced capabilities for materials modelling with Quantum ESPRESSO. *J. Phys. Condens. Matter* **29**, 465901 (2017).
42. Giannozzi, P. et al. QUANTUM ESPRESSO: a modular and open-source software project for quantum simulations of materials. *J. Phys. Condens. Matter* **21**, 395502 (2009).
43. Perdew, J. P., Burke, K. & Ernzerhof, M. Generalized gradient approximation made simple. *Phys. Rev. Lett.* **77**, 3865–3868 (1996).
44. Monkhorst, H. J. & Pack, J. D. Special points for Brillouin-zone integrations. *Phys. Rev. B* **13**, 5188 (1976).
45. Zhang, Y., Sun, J., Perdew, J. P. & Wu, X. Comparative first-principles studies of prototypical ferroelectric materials by LDA, GGA, and SCAN meta-GGA. *Phys. Rev. B* **96**, 035143 (2017).
46. Kolpak, A. M., Sai, N. & Rappe, A. Short-circuit boundary conditions in ferroelectric $PbTiO_3$ thin films. *Phys. Rev. B* **74**, 054112–054117 (2006).
47. Leferovich, R. P. & Mitchell, R. H. A structural study of ternary lanthanide orthoscandate perovskites. *J. Solid State Chem.* **177**, 2188–2197 (2004).
48. Longo, V. M. et al. On the photoluminescence behavior of samarium-doped strontium titanate nanostructures under UV light. A structural and electronic understanding. *Phys. Chem. Chem. Phys.* **12**, 7566–7579 (2010).
49. Bansal, C., Kawanaka, H., Takahashi, R. & Nishihara, Y. Metal–insulator transition in Fe-substituted $SrRuO_3$ bad metal system. *J. Alloys Compd.* **360**, 47–53 (2003).
50. Kuroiwa, Y., Aoyagi, S. & Sawada, A. Evidence for Pb-O covalency in tetragonal $PbTiO_3$. *Phys. Rev. Lett.* **87**, 217601–217605 (2001).
51. Jones, L. et al. Smart Align—a new tool for robust non-rigid registration of scanning microscope data. *Adv. Struct. Chem. Imaging* **1**, 8 (2015).
52. Li, Q. et al. Quantification of flexoelectricity in $PbTiO_3/SrTiO_3$ superlattice polar vortices using machine learning and phase-field modeling. *Nat. Commun.* **8**, 1468 (2017).
53. Aso, R., Kan, D., Shimakawa, Y. & Kurata, H. Octahedral tilt propagation controlled by A-site cation size at perovskite oxide heterointerfaces. *Cryst. Growth Des.* **14**, 2128–2132 (2014).
54. Peters, J. J. P. et al. Polarization screening mechanisms at $La_{0.7}Sr_{0.3}MnO_3$–$PbTiO_3$ interfaces. *ACS Appl. Mater. Interfaces* **12**, 10657–10663 (2020).
55. Sanchez-Santolino, G. et al. Oxygen octahedral distortions in $LaMO_3/SrTiO_3$ superlattices. *Microsc. Microanal.* **20**, 825–831 (2014).
56. Rondinelli, J. M. & Spaldin, N. A. Structure and properties of functional oxide thin films: insights from electronic-structure calculations. *Adv. Mater.* **23**, 3363–3381 (2011).
57. Sepliarsky, M., Stachiotti, M. G. & Migoni, R. L. Surface reconstruction and ferroelectricity in $PbTiO_3$ thin films. *Phys. Rev. B* **72**, 014110–014116 (2005).
58. Zhang, S. et al. Polarization rotation in ultrathin ferroelectrics tailored by interfacial oxygen octahedral coupling. *ACS Nano* **12**, 3681–3688 (2018).

Acknowledgements This work was partly supported by the EPSRC (UK) through grant nos. EP/P031544/1 and EP/P025803/1. M.A. acknowledges the Theo Murphy Blue Skies Award of the Royal Society. This research used resources of the Advanced Photon Source, a US Department of Energy (DOE) Office of Science user facility, operated for the DOE Office of Science by Argonne National Laboratory under contract no. DE-AC02-06CH11357. We also acknowledge the technical support from M. Crosbie. We would like to acknowledge the University of Warwick Research Technology Platform for assistance in the research described in this paper.

Author contributions M.A. conceived the idea. D.R., M.A. and A.M.S. designed the experiments. D.R. prepared the samples, performed DFT and DF-TEM experiments and analysed the data. J.J.P.P. and J.A.G. performed the STEM experiments and analysis. G.A.A.N., J.S., D.H. and D.R. collected the synchrotron data. T.P.A.H. and D.R. analysed the XRD data. R.B. performed the two-beam diffraction contrast simulations. All authors contributed to the discussions. All authors wrote the manuscript.

Competing interests The authors declare no competing interests.

Additional information

Supplementary information The online version contains supplementary material available at https://doi.org/10.1038/s41586-021-04260-1.

Correspondence and requests for materials should be addressed to Marin Alexe.

Peer review information *Nature* thanks the anonymous reviewers for their contribution to the peer review of this work.

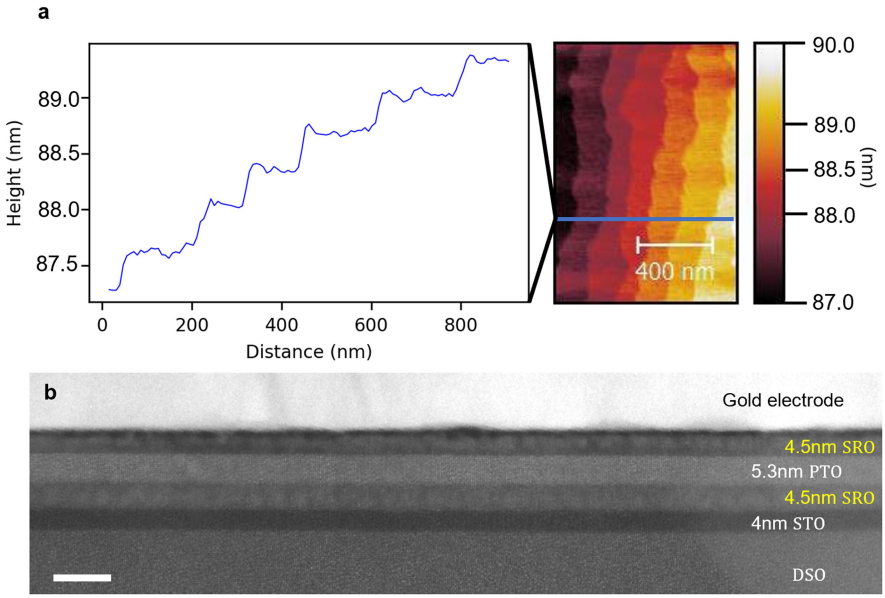

Extended Data Fig. 1 | Structure characterization. a, AFM topography of the surface of our $(SrRuO_3)_{11}/(PbTiO_3)_{13}/(SrRuO_3)_{11}$ trilayer sample. **b**, Low-magnification cross-sectional STEM of the sample. The scale bar is 10 nm.

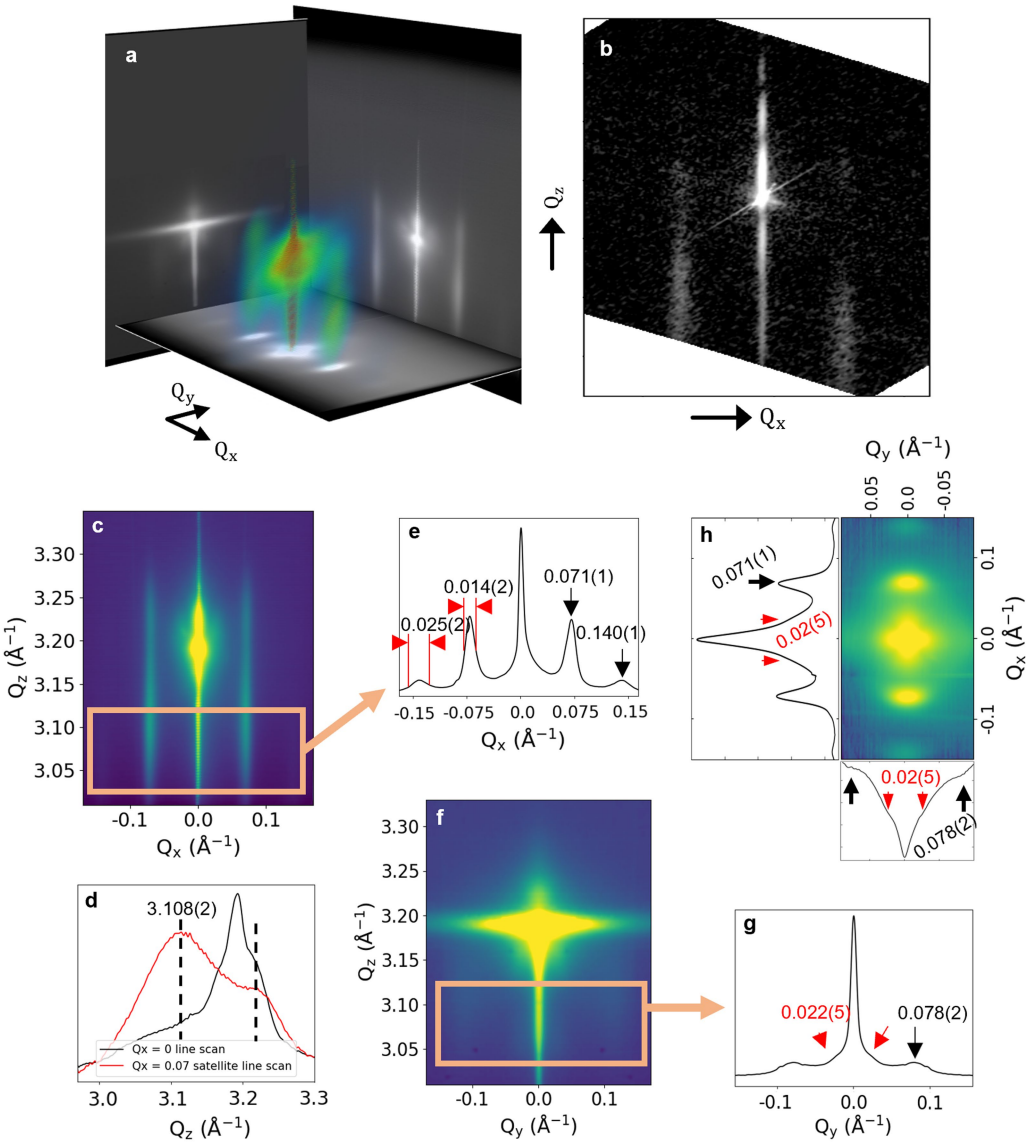

Extended Data Fig. 2 | RSM data. a, 3D reciprocal space map around the DSO 002_{pc} Bragg peak. The side panels show the 2D projected intensity of the recorded scatter. **b**, RSM around the asymmetric reflection $(103)_{pc}$. **c**, Reciprocal space map Q_z versus Q_x. **d**, Comparison plot of the extracted Q_z scan at $Q_x = 0$ and $Q_x = 0.07$ Å^{-1}. **e**, Integrated (boxed area) line profile showing the first-order and second-order satellite peaks and their widths. **f**, Reciprocal space map Q_z versus Q_y. **g**, The integrated (boxed area) line profile shows weak first-order satellite peaks corresponding to a periodicity of about 8.05 nm. **h**, Plan-view projection into a Q_x versus Q_y RSM map with extracted line scans showing the in-plane distribution of the satellite peaks.

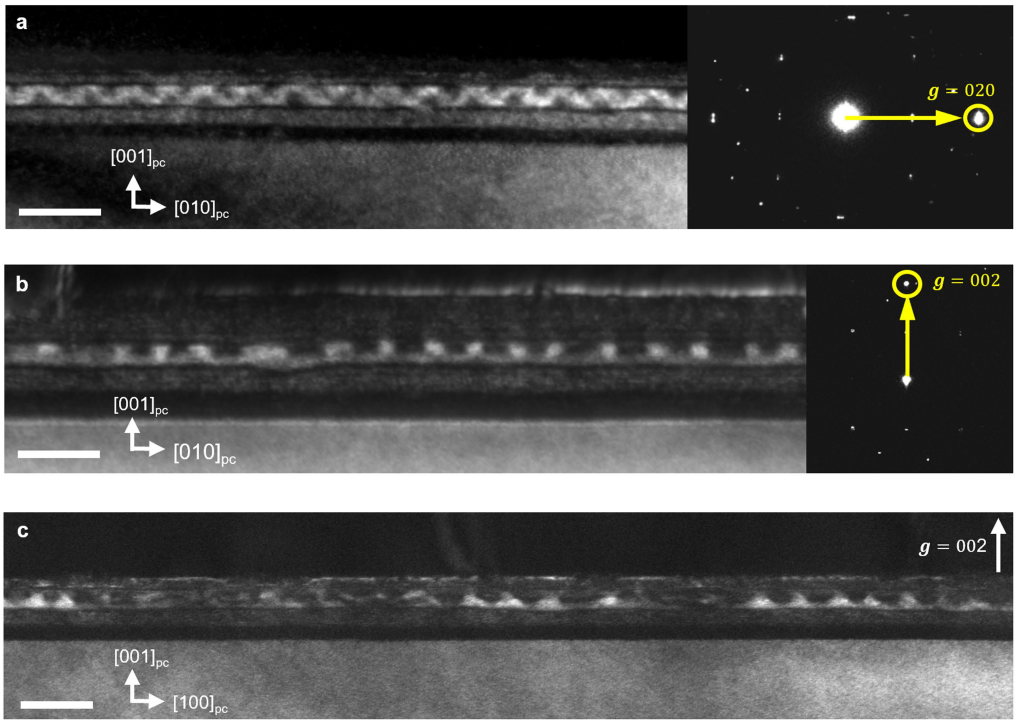

Extended Data Fig. 3 | Cross-sectional DF-TEM. a, Image of a $(100)_{pc}$ cross section taken under the $\mathbf{g} = 020_{pc}$ excitation condition. **b**, Image of the same $(100)_{pc}$ cross section taken under the $\mathbf{g} = 002_{pc}$ excitation. **c**, Image of a $(010)_{pc}$ cross section (that is, cut at 90° from **a** and **b**) taken using $\mathbf{g} = 002_{pc}$. The scale bars are 20 nm.

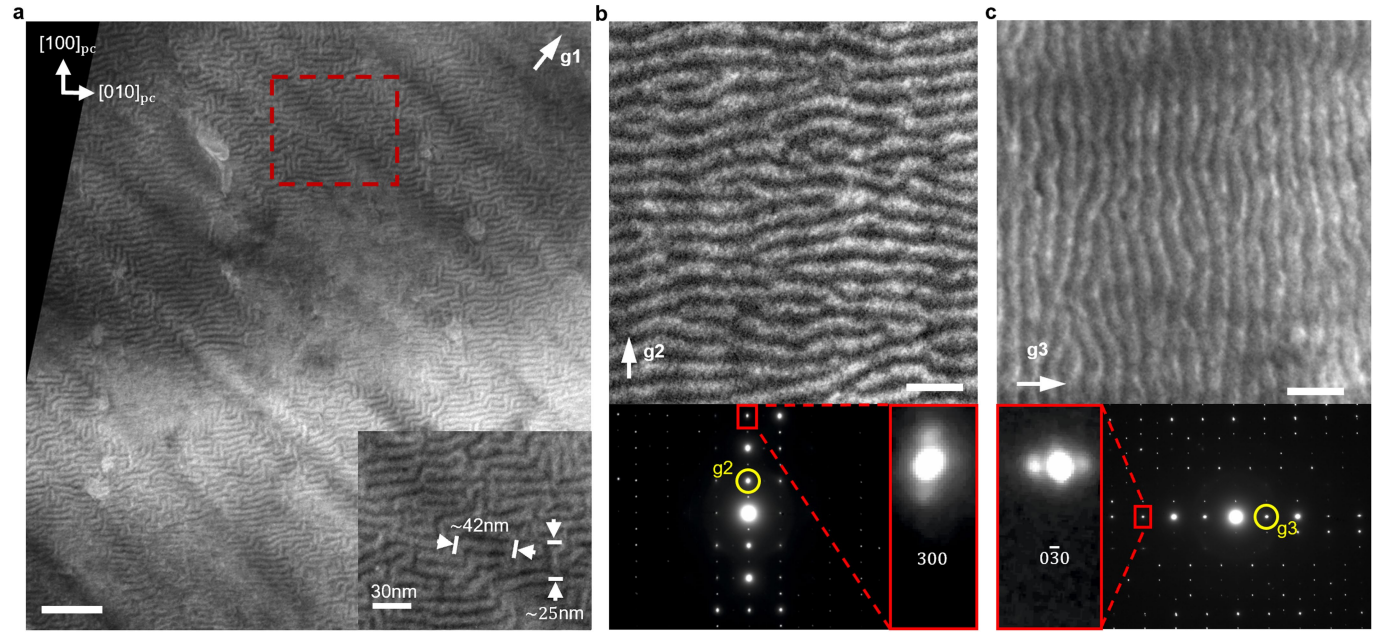

Extended Data Fig. 4 | Plan-view DF-TEM. a, Low-magnification plan view of the complex domain pattern take under the $\mathbf{g}_1 = 110_{pc}$ condition. The figure inset shows the enlarged boxed area. **b**, Plan-view dark-field image taken under $\mathbf{g}_2 = 100_{pc}$. **c**, Plan-view diffraction contrast taken under $\mathbf{g}_3 = 010_{pc}$ excitation. The scale bars are 100 nm for **a** and 30 nm for **b** and **c**.

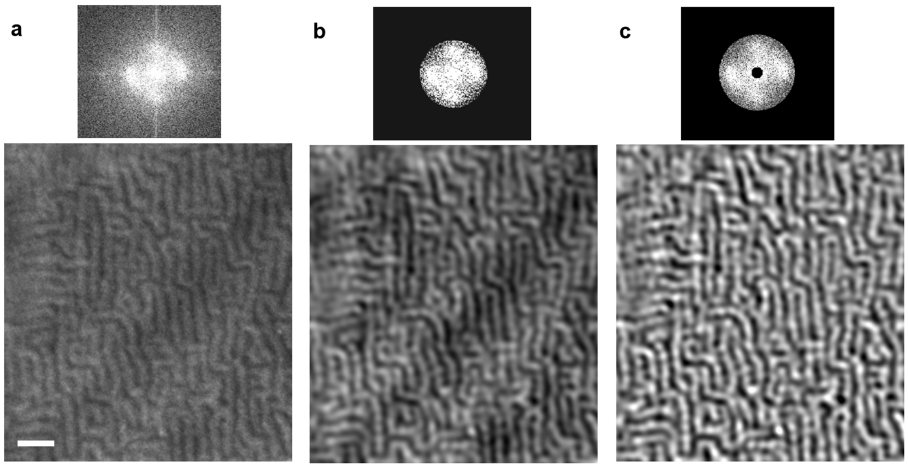

Extended Data Fig. 5 | Noise filter. a, 2D Fourier transform of the plan-view image taken under $\mathbf{g}_1 = 110$ excitation. **b**, Bandpass filter that removes the noise and retains the signal for $|\mathbf{Q}| < 0.16\ \mathrm{nm}^{-1}$. **c**, Bandpass filter that also removes the central spot and the signal for $|\mathbf{Q}| < 0.015\ \mathrm{nm}^{-1}$. The scale bar is 30 nm.

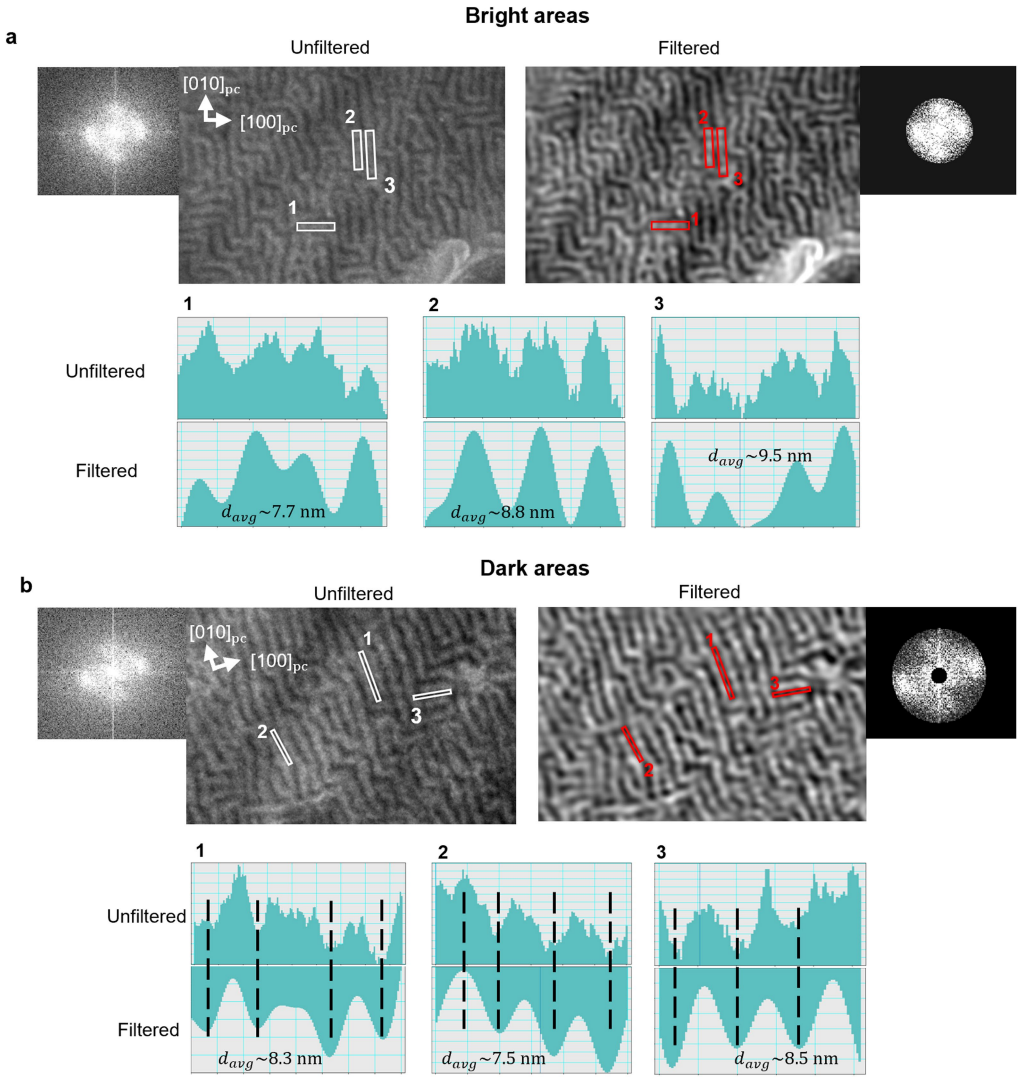

Extended Data Fig. 6 | Filtered/unfiltered plan-view DF-TEM. a, The bandpass filter improves the signal-to-noise ratio without introducing artefacts. Both the filtered and unfiltered images show, apart from the labyrinth pattern, a periodic modulation in the contrast along the individual domains. **b**, The second modulation permeates the labyrinth pattern.

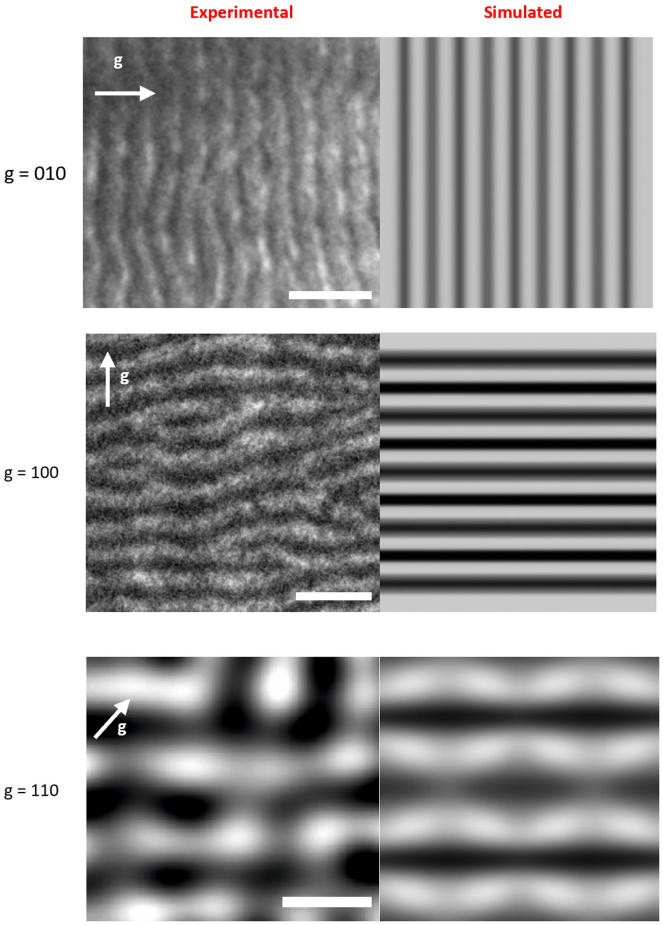

Extended Data Fig. 7 | Diffraction contrast simulations. Left, experimental plan-view DF-TEM images of the vortex array. Note that the $\mathbf{g} = 110_{pc}$ image is at higher magnification and Bragg filtered. Right, two-beam Howie–Whelan diffraction contrast simulations of the contrast arising from the strain fields of a 2D array of vortices as described in the main text (deviation parameter $s = 0.01$ nm). The scale bars are 30 nm for $\mathbf{g} = 010$, 30 nm for $\mathbf{g} = 100$ and 10 nm for $\mathbf{g} = 110$.

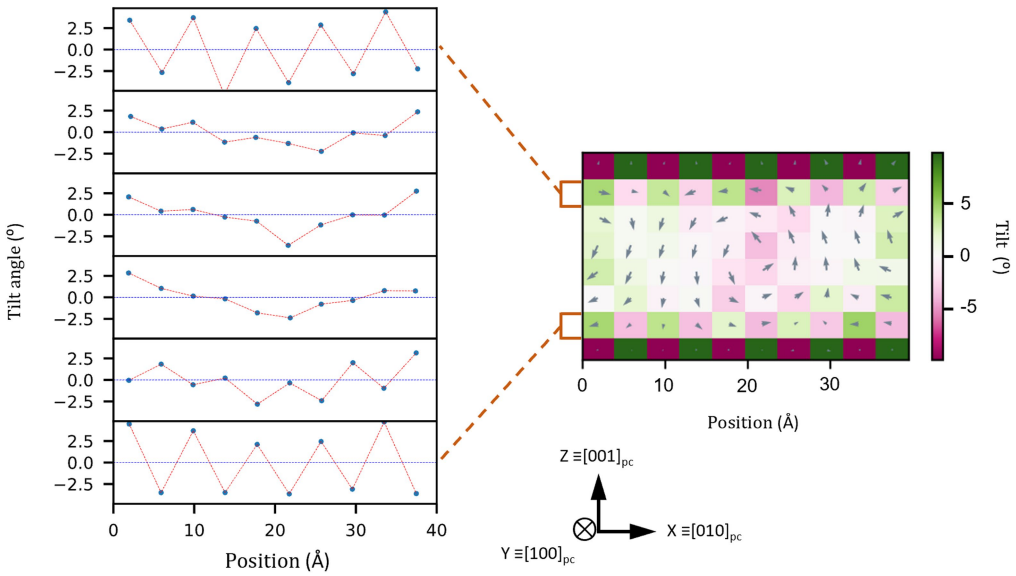

Extended Data Fig. 8 | Tilt map. Left, oxygen tilt behaviour along a row of unit cells. Right, tilt map throughout the PTO layer.

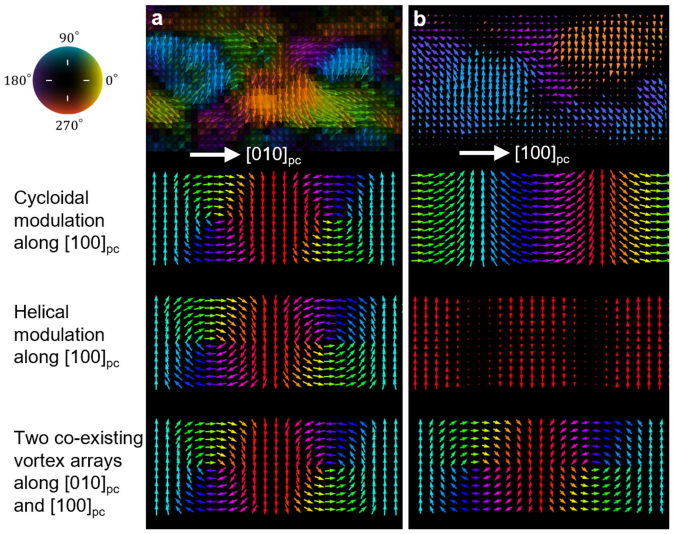

Extended Data Fig. 9 | Cross-sectional polar maps. a, Polarization maps along the ordered $[010]_{pc}$ direction. The projection of a cycloidal and helical modulated vortex array into the $[001]_{pc}$–$[010]_{pc}$ plane shows that the domain topology is retained. **b**, The projection of the modulated vortex array into the $[001]_{pc}$–$[100]_{pc}$ plane shows that the cycloidal modulation allows the polar vector to rotate in plane, similar to the experimental polar map, whereas the helical modulation does not.

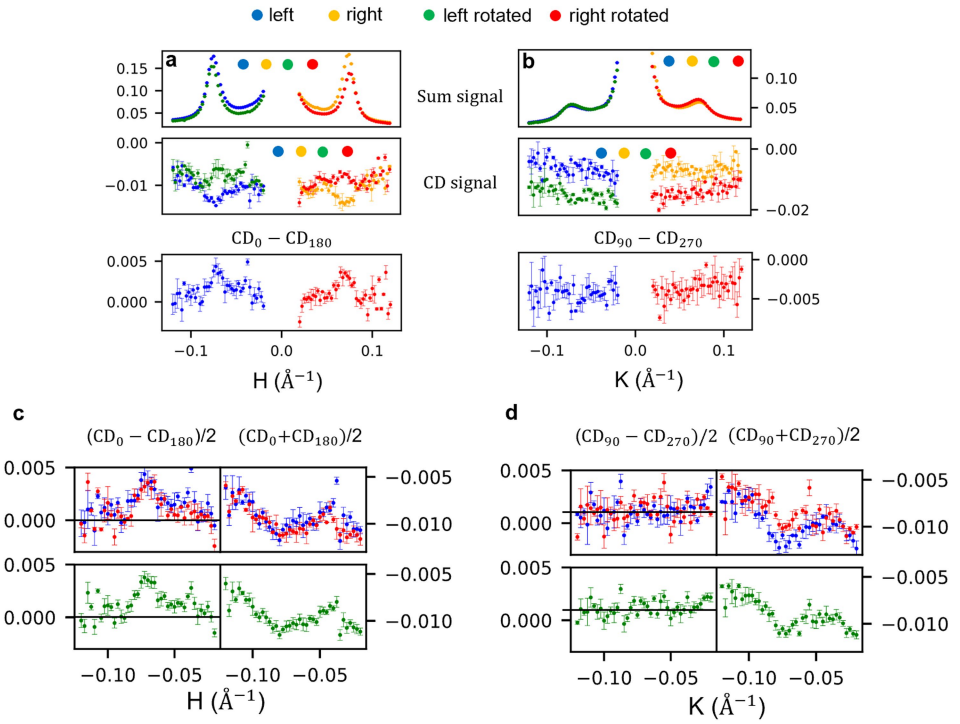

Extended Data Fig. 10 | X-ray CD data. a, $[100]_{pc}//[001]_o$ in the scattering plane. **b**, $[010]_{pc}//[-110]_o$ in the scattering plane. The first row presents the sum of the dichroic signal, $(I^+ + I^-)/2$, in which $I^{\pm}$ refers to the measured intensity for opposite helicities of the incoming light and the second row shows the CD signal, $(I^+ - I^-)/(I^+ + I^-)$, and its behaviour on 180° rotation of the sample. The third panel shows the dichroic signal, $(CD_{\phi 1} - CD_{\phi 2})/2$, associated with a rotation of the sample by 180°, demonstrating a weak signal at the ± satellites in **a**, which is absent in **b**. In **c** and **d**, we show the dichroism under sample rotation when $[100]_{pc}//[001]_o$ is in the scattering plane (**c**) and when the $[010]_{pc}//[-110]_o$ direction is in the scattering plane (**d**). The upper panels of **c** and **d** plot the data from the two satellites onto a common axis, with the lower panels showing their average.